An S/T motif controls reversible oligomerization of the Hsp40 chaperone DNAJB6b through subtle reorganization of a β sheet backbone

Theodoros K. Karamanos[a,1], Vitali Tugarinov[a], and G. Marius Clore[a,2]

[a]Laboratory of Chemical Physics, National Institute of Diabetes and Digestive and Kidney Diseases, National Institutes of Health, Bethesda, MD 20892

Contributed by G. Marius Clore, October 15, 2020 (sent for review September 28, 2020; reviewed by Hashim M. Al-Hashimi and Lewis E. Kay)

Chaperone oligomerization is often a key aspect of their function. Irrespective of whether chaperone oligomers act as reservoirs for active monomers or exhibit a chaperoning function themselves, understanding the mechanism of oligomerization will further our understanding of how chaperones maintain the proteome. Here, we focus on the class-II Hsp40, human DNAJB6b, a highly efficient inhibitor of protein self-assembly in vivo and in vitro that forms functional oligomers. Using single-quantum methyl-based relaxation dispersion NMR methods we identify critical residues for DNAJB6b oligomerization in its C-terminal domain (CTD). Detailed solution NMR studies on the structure of the CTD showed that a serine/threonine-rich stretch causes a backbone twist in the N-terminal β strand, stabilizing the monomeric form. Quantitative analysis of an array of NMR relaxation-based experiments (including Carr–Purcell–Meiboom–Gill relaxation dispersion, off-resonance $R_{1\rho}$ profiles, lifetime line broadening, and exchange-induced shifts) on the CTD of both wild type and a point mutant (T142A) within the S/T region of the first β strand delineates the kinetics of the interconversion between the major twisted-monomeric conformation and a more regular β strand configuration in an excited-state dimer, as well as exchange of both monomer and dimer species with high-molecular-weight oligomers. These data provide insights into the molecular origins of DNAJB6b oligomerization. Further, the results reported here have implications for the design of β sheet proteins with tunable self-assembling properties and pave the way to an atomic-level understanding of amyloid inhibition.

Hsp40 chaperones | relaxation-based NMR | short-lived excited states | conformational transitions | oligomerization

In the complex environment of the cell, proteins often require the assistance of chaperones to maintain their functional state (1–3). Molecular chaperones facilitate the retention of the native conformation of their protein substrates throughout their lifetime by promoting correct folding and by preventing the formation and/or enhancing the degradation of misfolded/aggregated states (4). A vital component of the proteostasis network is the Hsp40(DNAJ)-Hsp70 system that performs critical housekeeping functions and is also up-regulated under stress (5, 6). In addition to delivering substrates to and enhancing the adenosine triphosphate cycle of the Hsp70 macromolecular machine, a number of Hsp40s have recently been shown to possess strong chaperone activity in their own right (5). In particular, the class-II Hsp40 DNAJB6b, the focus of the current paper, is a strong suppressor of protein self-assembly both in vivo and in vitro (7–9), and is associated with a number of human pathologies including cancer (10), myopathies (11), and viral infection (12). Interestingly, it is common for chaperones that prevent untoward protein aggregation, including DNAJB6b, to form oligomeric assemblies themselves (9, 13, 14). Whether the chaperone oligomers act as reservoirs for active monomers or represent the active chaperone configuration, it is important to understand the mechanisms of chaperone oligomerization in atomic detail to be able to tune the response of the chaperone network.

We have recently shown that DNAJB6b oligomerizes using interactions mediated through its C-terminal domain (CTD) (15) while the Ser/Thr-rich (S/T) domain directly N-terminal to the CTD modulates oligomerization (7, 15) (Fig. 1). The S/T domain contains one or more serine or threonine residues in 17 distinct sites in its sequence (termed ST1–ST17) (Fig. 1), with some sites being more important for chaperone activity than others (16) and S16/S17 being part of the N-terminal strand of the CTD domain (15) (Fig. 1). Oligomers of DNAJB6b are heterogeneous in size, ranging from 2 to 40 subunits, with a significant population of monomer also present (9, 15). Native oligomers are thought to be important for DNAJB6b-mediated inhibition of amyloid aggregation (7, 16); however, the origin of the heterogeneity in oligomer size and the mechanism of oligomerization remain unknown. Here we focus on the single β sheet CTD domain of DNAJB6b using a variety of relaxation-based NMR techniques and identify key residues that control the reversible oligomerization of DNAJB6b. We then solve the solution NMR structure of the CTD domain and show that the N-terminal B1 strand in the monomer, which contains ST16 and ST17, adopts a twisted conformation that prevents further aggregation. Upon increasing the concentration of the CTD domain, we observe the formation of a dimer accompanied by a transition of the B1 strand to a more regular β sheet conformation that facilitates higher-order oligomer formation. Importantly, the same set of residues

Significance

Some of the most potent chaperones that protect against protein aggregation form heterogeneous oligomers that are crucial for function. Due to the polydisperse nature of these oligomers, the molecular origins that drive self-assembly remain poorly understood. Here, using a predominantly monomeric construct of the C-terminal domain of DNAJB6b we reveal an interplay between two N-terminal β strand configurations which we analyze quantitatively in structural and kinetic terms. We show that the two backbone conformations impact the assembly state of the C-terminal domain, with one being essentially monomeric and the other prone to oligomerization. The same residues in full-length DNAJB6b are vital for antiaggregation activity and thus we hypothesize that the equilibria characterized here lie at the core of DNAJB6b function.

Author contributions: T.K.K., V.T., and G.M.C. designed research, performed research, analyzed data, and wrote the paper.

Reviewers: H.M.A., Duke University Medical Center; and L.E.K., University of Toronto.

The authors declare no competing interest.

[1]Present address: Astbury Centre for Structural Molecular Biology, School of Molecular and Cellular Biology, University of Leeds, LS2 9JT Leeds, United Kingdom.

[2]To whom correspondence may be addressed. Email: mariusc@mail.nih.gov.

This article contains supporting information online at https://www.pnas.org/lookup/suppl/doi:10.1073/pnas.2020306117/-/DCSupplemental.

First published November 16, 2020.

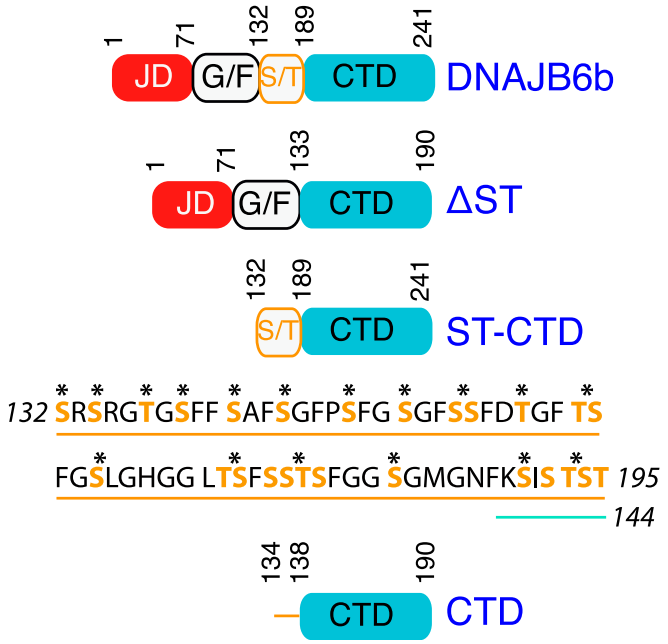

Fig. 1. Schematic of the domain organization of the constructs used in the current study. The sequence of the ST domain with the ST sites 1 to 17 in bold and marked with an asterisk is also shown. The ST16 and ST17 sites (residue 139 and residues 141 to 144 in the numbering of the ΔST-DNAJB6b construct) are also part of the CTD domain. The orange and cyan lines below the ST domain sequence refer to the ST and CTD domains, respectively.

identified here as switches for oligomerization have been shown to play a vital role in the inhibition of amyloid β aggregation by DNAJB6b (16). The results provide insights into how a single β sheet protein, with all its strands exposed, can exist in a monomeric form that exchanges with higher-order oligomers. The findings have clear implications for the design of β sheet proteins that self-assemble in a reversible manner upon stimulus and pave the way for an atomic-level description of the inhibition of nucleation events in amyloid formation by DNAJB6b.

Results and Discussion

Constructs Used in the Present Work. A summary of the constructs used in the present work and their relation to wild-type DNAJB6b is provided in Fig. 1. In the construct used in the previous work (15), ΔST-DNAJB6b, the S/T domain was deleted. Two constructs are studied here: ST-CTD and CTD. The former comprises the full S/T and CTD domains; the latter comprises only the CTD domain which includes sites ST16 and ST17 of the S/T domain located in strand B1 of the CTD domain.

Methyl-Based NMR Identifies Concentration-Dependent Exchange Processes in the Edge Strands of the CTD Domain. The ΔST-DNAJB6b construct studied previously is predominantly monomeric, transiently exchanging with a small population of high-molecular-weight oligomer (15). These studies were based on ^{15}N Carr–Purcell–Meiboom–Gill (CPMG) relaxation dispersion experiments involving residues in strand B5 that showed concentration-dependent CPMG profiles. A number of amide resonances in the ST16/ST17 region were either broadened beyond detection or overlapped in the ^{1}H-^{15}N correlation spectrum, and thus the role of the B1 edge strand in oligomerization could not be assessed using these data. However, ΔST-DNAJB6b contains numerous methyl-bearing side chains, including residues in the B1 and B4/B5 strands of the CTD whose resonances have been assigned previously (17).

We therefore performed methyl-based single-quantum (SQ) ^{13}C (18) and ^{1}H (19) relaxation experiments to probe the dynamics of methyl side chains in [ILV-^{13}CH$_3$/^{15}N/^{2}H]–labeled ΔST-DNAJB6b as a function of concentration (Fig. 2*A*). Residues in the J domain (JD) (Fig. 1) show essentially flat CPMG relaxation dispersion profiles, owing to the high degree of ordering within the hydrophobic core of this domain (20). Methyl groups of residues located in the B4/B5 strands of the CTD domain, however, display significant contributions from chemical exchange (R_{ex}, the difference in effective R_2 values between 0- and 2,000-Hz CPMG fields) to both their ^{13}C and ^{1}H transverse relaxation rates (Fig. 2 *A*, *Right* and *SI Appendix*, Figs. S1 and S2), in agreement with our previous ^{15}N-CPMG relaxation

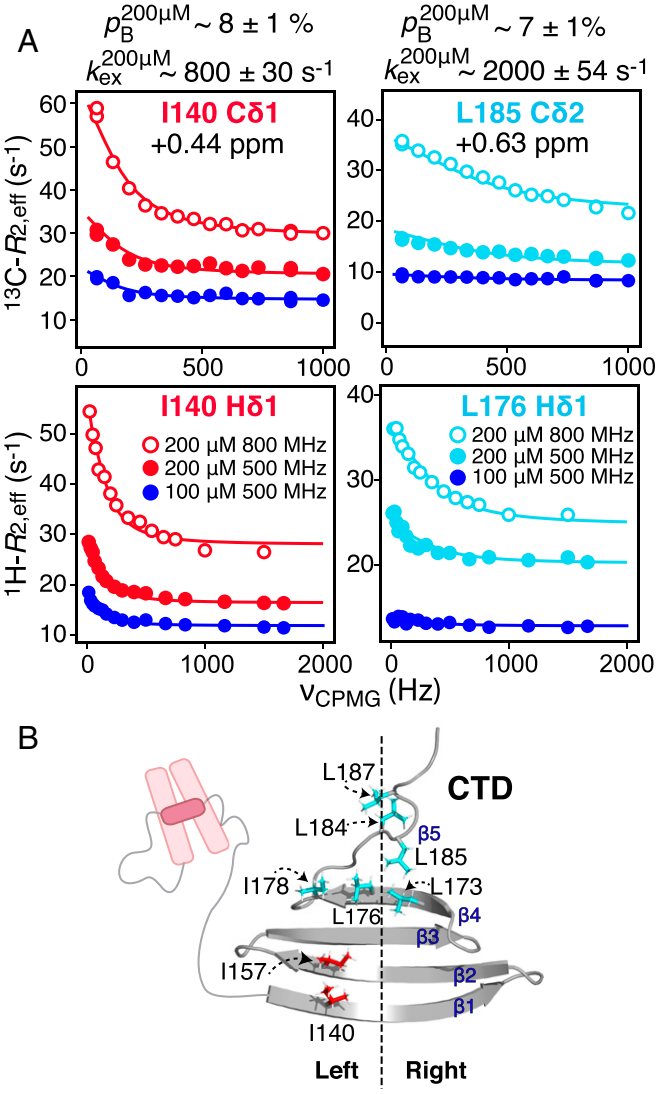

Fig. 2. Probing concentration-dependent exchange processes in ΔST-DNAJB6b using methyl-based NMR. (*A*) SQ methyl ^{13}C (*Top*) and ^{1}H (*Bottom*) CPMG relaxation dispersion data for [^{2}H/^{15}N/ILV-^{13}CH$_3$]–labeled ΔST-DNAJB6b at 298 K recorded at spectrometer ^{1}H frequencies of 500 (filled circles) and 800 (open circles) MHz and at two protein concentrations (100 μM, blue; 200 μM, red/cyan). Residues in the B1/B2 strands (*Left*) and in B4/B5 strands (*Right*) were fitted separately to a two-state model. The resulting exchange parameters at a concentration of 200 μM are listed above the panels. The fitted ^{13}C-Δω values that were used to determine the rotameric distribution in the oligomeric state are noted in *Top*. (*B*) Location of the two sets of residues in the B1/B2 (blue) and B4/B5 (cyan) strands highlighted as sticks on the structure of the CTD domain. The full datasets are shown in *SI Appendix*, Figs. S1 and S2.

dispersion data on ΔST-DNAJB6b (15). Further, methyl groups in the N-terminal portion of strand B1 and the C-terminal end of strand B2 (which constitute the "left" side of the CTD as displayed in Fig. 2*B*) also show large R_{ex} terms (Fig. 2 *A*, *Left*). The ^{13}C and ^{1}H R_{ex} terms are concentration-dependent (Fig. 2*A*) and, under the conditions employed, the calculated R_2 rates for the minor state (R_2^B) are 10 to 15 times larger than those of the monomer, reflecting exchange with a high-molecular-weight oligomeric state. The apparent increase in R_{ex} observed for ΔST-DNAJB6b when only the slow relaxing ^{1}H transitions of the $I = 1/2$ manifold of the methyl groups are selected before the CPMG sequence (21) further indicates exchange with a slowly tumbling species.

The SQ methyl ^{1}H and ^{13}C CPMG relaxation dispersion data for the CTD domain could not be fitted globally to the same exchange process (Fig. 2*A*). The methyl groups in the B1/B2 strand can be fit to a two-site exchange process with an overall exchange rate k_{ex} ($= k_{on} + k_{off}$) of ~800 s^{-1} with a population (p_B) of ~8% for the minor state at a concentration of 200 μM (Fig. 2 *A*, *Left*). The methyl groups in strands B4/B5 can also be fit to a two-site exchange process that is significantly faster (k_{ex} ~2,000 s^{-1} and p_B ~7% at the same concentration; Fig. 2 *A*, *Right*). These data suggest the existence of complex equilibria related to oligomer formation that involve the edge strands of the CTD domain.

For the ^{13}C resonances of Ile140 Cδ1 (+0.44 ppm) and Leu185 Cδ1 (−0.31 ppm)/Cδ2 (+0.63 ppm) for which the sign of the chemical shift difference between the monomeric and oligomeric state could be obtained (by comparing ^{1}H-^{13}C heteronuclear multiple quantum correlation spectra at low and high concentrations) the χ_2 rotameric distribution of the side chain in the minor (oligomeric) state can be derived (22–24) and compared with the rotameric populations obtained by analysis of ^{1}H-^{13}C residual dipolar couplings (RDCs) in the monomeric form (17). χ_2 for Ile140 has a *gauche*-/*trans* distribution (p_g-/p_t) of 0.12/0.88 in the oligomer compared to 0.22/0.78 in the monomer. Leu185 shows a χ_2 rotameric distribution very close to that expected in a random coil ($p_t = 0.65$) (25) in the monomer, which changes to $p_t = 0.55$ in the oligomer. The chemical shift data derived from the methyl CPMG relaxation dispersion data suggest that the methyl-containing side chains of strands B1 and B4/B5 become more rigid upon oligomerization.

The Isolated CTD Domain Is Monomeric at Low Concentrations and the S/T Domain Shifts the Equilibrium to Oligomers. The relaxation dispersion data on the ΔST-DNAJB6b construct in Fig. 2 points to regions of the CTD that are important for oligomerization. However, the ~23-kDa size of ΔST-DNAJB6b combined with significant resonance overlap require the use of deuteration that limits the available probes to amide or methyl protons, with backbone amides of residues in strand B1 displaying increased line broadening. Another complication arises from the fact that transient interactions between the JD and CTD also take place on the millisecond timescale (15), further complicating the interpretation of CPMG relaxation dispersion data. We therefore designed two constructs, ST-CTD and CTD (Fig. 1), to focus on the oligomerization process.

While the CTD construct, perhaps surprisingly for a single β sheet protein, is largely monomeric as judged by analytical size-exclusion chromatography (Fig. 3*A*), dynamic light scattering and sodium dodecyl sulfate polyacrylamide gel electrophoresis (SDS/PAGE) on the ST-CTD construct are indicative of a heterogeneous pool of oligomers (Fig. 3 *B* and *C*) similar to that formed by wild-type DNAJB6b (9). ^{15}N-R_2 relaxation measurements on the CTD construct (Fig. 3*D*) reveal a number of residues associated with loops that show significantly higher R_2 values than the rest of the protein at 298 K (Fig. 3*E*). The variation in R_2 values is somewhat decreased when the temperature is reduced to 283 K, suggesting that there is a fast exchange process affecting the loops connecting the β strands that is not fully suppressed by the applied spin-lock field (1.5 and 1.75 kHz at 298 and 283 K, respectively). Excluding the flexible regions, model-free Lipari–Szabo analysis (26–28) yields an overall

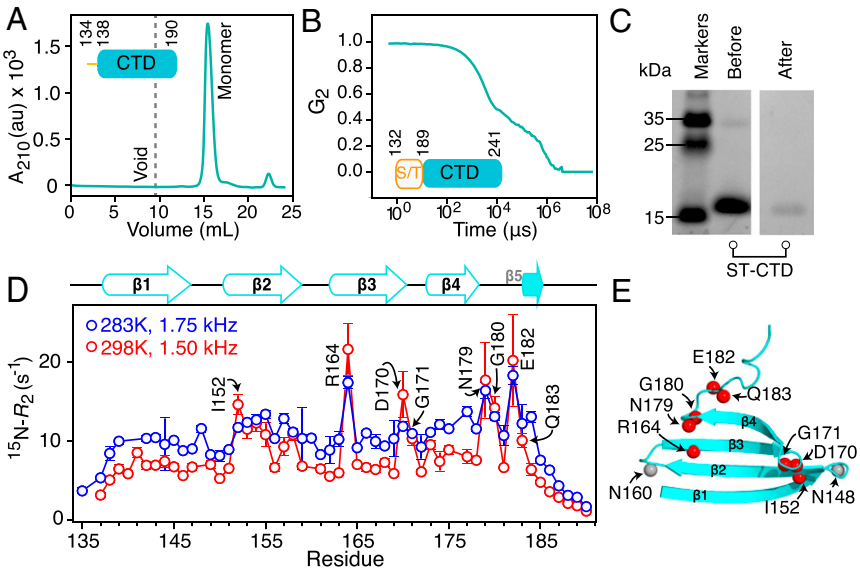

Fig. 3. The isolated CTD domain is monomeric at low concentration while the ST-CTD construct forms heterogenous oligomers. (*A*) Analytical size-exclusion chromatography of 100 μM CTD. (*B*) Dynamic light scattering time correlation function and (*C*) SDS/PAGE before and after centrifugation at 16,000 × *g* of 100 μM ST-CTD in 20 mM sodium phosphate, pH 7.5, and 300 mM NaCl. After pelleting the oligomer by centrifugation, the band intensity for the CTD left in the supernatant is significantly reduced. (*D*) ^{15}N-R_2 profile for 120 μM [$^{15}N/^{13}C/^{2}H$]-labeled CTD at 298 and 283 K (red and blue circles, respectively). (*E*) Residues that show significantly larger ^{15}N-R_2 values are highlighted and their nitrogen atom positions are shown as red spheres on the structure of the CTD domain (Protein Data Bank ID code 6U3S). Residues 148 and 160 (shown as gray spheres) are broadened beyond detection in the ^{1}H-^{15}N HSQC spectrum of the CTD domain.

correlation time (τ_c) of 4.0 ± 0.3 ns with a diffusion anisotropy ($D_{||}/D_{\perp}$) of 1.74 ± 0.12 at 298 K, fully consistent with a 6.5-kDa monomeric protein.

The Refined Solution Structure of the Isolated CTD Domain Reveals a Twisted B1 Strand. The small size and excellent quality of the CTD NMR spectra allow a complete NMR-based structural investigation of the original CS-Rosetta (29) structural model that only made use of backbone chemical shifts supplemented by sparse experimental NMR restraints (15). Resonances of the ST16/ST17 sites in the N-terminal part of B1 that were broadened beyond detection in ΔST-DNAJB6b are visible in the CTD construct, allowing a detailed characterization of this region of the protein. Analysis of the assigned backbone chemical shifts shows that the ST16/ST17 adopt unusual ϕ/ψ angles as reflected by the β strand propensity calculated using the program Talos+ (30) (Fig. 4*A*). A set of 225 nuclear Overhauser enhancement (NOE)-derived interproton distance restraints (73 involving the B1 strand), together with chemical shift-derived backbone ϕ/ψ torsion angle restraints and one-bond $^1D_{NH}$ and $^1D_{CH}$ RDC (*SI Appendix*, Table S1), were used to refine the CS-ROSETTA structure of the CTD by simulated annealing using the program Xplor-NIH (31). The backbone precision of the resulting structure is ∼0.6 Å (rms to the mean coordinate positions) with a Cα displacement of ∼1.5 Å to the original CS-Rosetta structure (Fig. 4*B*). The most striking difference between the two structures is related to the ST16/ST17 sites in the B1 strand (Fig. 4*C*). In the original CS-Rosetta structure (15) the B1 strand adopts a regular β strand conformation (termed "straight") in which all twist angles (defined in Fig. 4*D*) are positive (with one exception at −2°; Fig. 4*C*), leading to the common (canonical) slightly positive twist of β strands. The refined structure of the isolated CTD domain, however, shows a negative and positive twist centered around I140 and T142A, respectively, that leads to a rearrangement of the H-bond donors and acceptors in the N-terminal portion of strand B1 (Fig. 4*C*). Although the twisted B1 conformation does not necessarily give rise to a distinct NOE pattern, it is best reflected in the backbone torsion angle and $^1D_{CH}$ RDC data. For example, the side chain of Thr142 experiences an almost 180° rotation resulting in a large negative $^1D_{CH}$ value for the Cβ-Hβ bond vector in the twisted configuration, in contrast to a close to zero value for the straight B1 conformation (Fig. 4*E*). Similar observations for other C–H bond vectors in the B1 strand are shown in Fig. 4*F* (agreement between observed and calculate backbone amide RDCs is shown in Fig. 4*G*). Twisting of the B1 strand is also accompanied by an increase in bending angles that change signs (32) around Thr142 (Fig. 4 *C* and *D*), as well as a shortening of the B2 and B3 strands at their C and N termini, respectively, that are in close proximity to the ST16/ST17 sites in strand B1 (Fig. 4*B*). An independent validation is provided by the measurement of $^3J_{HN\text{-}H\alpha}$ scalar couplings that report exclusively on the backbone ϕ torsion angle. The $^3J_{HN\text{-}H\alpha}$ couplings for residues in strand B1 are shown in *SI Appendix*, Fig. S3 and show slightly better agreement with the twisted configuration rather than a straight B1 strand.

The twisted conformation of the B1 strand already provides clues about how the isolated CTD domain resists aggregation despite its single β sheet fold; twisting alters the angles of bond vectors that would be predisposed to form intermolecular hydrogen bonds with the strands of another CTD monomer if the B1 strand adopted a straight configuration (33). In this regard, mutation of the ST16/ST17 sites to alanine, which would be expected to alter the oligomerization equilibria, retains the oligomeric form of DNAJB6b but dramatically decreases the ability of DNAJB6b to inhibit amyloid β aggregation (16).

The Isolated CTD Domain Shows Extensive Dynamics Related to Oligomerization. Our previous data (15), as well as those shown in Fig. 2, show that ΔST-DNAJB6b undergoes exchange with large oligomeric species. To probe the oligomerization of the isolated CTD domain, we monitored ^{15}N and $^{13}C\alpha$ chemical shifts and performed ^{15}N-based relaxation experiments over a series of concentrations in which the total protein concentration was varied from 20 μM to 1.3 mM. At concentrations below 300 μM the integrated volume of the first increment of the ^1H-^{15}N and ^1H-^{13}C correlation spectra correlates linearly with the total CTD concentration as expected for a soluble protein that does not self-assemble. However, as the total CTD concentration is increased above 300 μM, saturation of the integrated cross-peak intensities is observed, indicative of the formation of high-molecular-weight species whose magnetization fully relaxes during the two INEPT transfer periods (7 to 10 ms) employed in both heteronuclear correlation experiments (34) (*SI Appendix*, Fig. S4*A*). Fitting to a power-law function revealed an approximately quadratic relationship between the concentrations of NMR-visible and NMR-invisible CTD (*SI Appendix*, Fig. S4*B*). Consistent with data on full-length DNAJB6b that forms spherical heterogeneous oligomers (9), dynamic light scattering experiments on the CTD construct at a total concentration of 1.3 mM confirm the presence of large particles (with an average diameter of ∼8 nm) that are difficult to characterize further due to their low molar concentration (*SI Appendix*, Fig. S4*C*). To quantitatively analyze the NMR data, we therefore only consider the concentration of the NMR-visible species (*SI Appendix*, *SI Materials and Methods*). During the titration the ^{15}N chemical shifts of residues in proximity to the ST16/ST17 sites and B5 strand scale linearly with the concentration of NMR-visible CTD species (Fig. 5*A*, two right-most panels and *SI Appendix*, Fig. S5*A*). This is accompanied by an increase in the ^{15}N-R_2 values (^{15}N-ΔR_2) which show a nonlinear concentration dependence with characteristic curvature indicative of the formation of higher-order species (Fig. 5*A*, two left-most panels and *SI Appendix*, Fig. S5*B*).

To investigate the concentration-dependent equilibria involving the CTD domain we also performed off-resonance ^{15}N-$R_{1\rho}$ experiments in the rotating frame (35) (Fig. 5*B* and *SI Appendix*, Fig. S6). For residues that do not exhibit a chemical shift difference between the ground and excited states, the profiles of ^{15}N-$R_{2,\text{eff}}$ as a function of offset frequency have an "inverted" appearance and, in addition, shift toward higher $R_{2,\text{eff}}$ values at higher protein concentrations, both characteristic of exchange with a slowly tumbling species (35).

^{15}N-CPMG relaxation dispersion experiments show large profiles for residues in the ST16/ST17 sites, suggesting that they undergo exchange with an alternative conformation (Fig. 5*C* and *SI Appendix*, Fig. S7). This conformational change is concentration-dependent (Fig. 5*D* and *SI Appendix*, Figs. S7 and S8) and is transmitted across the entire "left" side of the CTD domain (Fig. 2*B*) with residues in this area also showing significant R_{ex} terms (Fig. 5*C* and *SI Appendix*, Fig. S9 *A* and *B*). Similar to the ΔST-DNAJB6b construct, we also observed smaller, concentration-dependent ^{15}N-CPMG relaxation dispersion profiles for residues located in strand B5 (Fig. 5 *C* and *D*) that presumably reflect the docking of the C-terminal B5 strand to strand B4. Thus, the ^{15}N-CPMG relaxation dispersion data for both strands B1 and B5 probe concentration-dependent phenomena and not the interconversion between different conformations of the monomer.

Kinetics of the CTD Oligomerization Pathway. To obtain quantitative information about the kinetics of the exchange process from monomeric to oligomeric CTD, we simultaneously fit the following NMR data (*SI Appendix*, Table S2 and Figs. S5–S7) to a variety of kinetic schemes (Table 1): ^{15}N-CPMG relaxation dispersion profiles at NMR-visible CTD concentrations of 80 and 240 μM, off-resonance ^{15}N-$R_{1\rho}$ data at NMR-visible CTD concentrations of 240 and 800 μM, and exchange-induced shifts (δ_{ex}) and ^{15}N-ΔR_2 data spanning a total CTD concentration range of

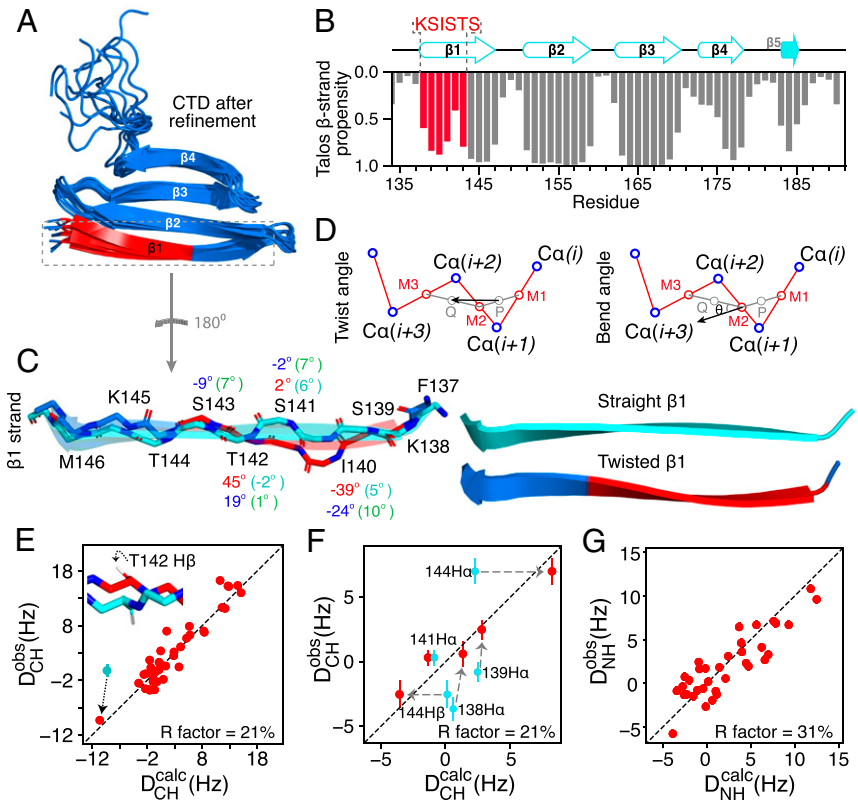

Fig. 4. The B1 strand of the CTD domain monomer is twisted. (*A*) Secondary structure propensity of the CTD domain deduced from the backbone chemical shifts using the program TALOS+ (30). The S/T motif is indicated by the red bars with its sequence shown at the top. (*B*) Ensemble of the 10 lowest-energy structures after Xplor-NIH (31) refinement using NOE-derived interproton distance, φ/ψ dihedral angle, and RDC ($^1D_{CH}$ and $^1D_{NH}$) restraints. A summary of the structural statistics is provided in *SI Appendix*, Table S1. (*C*) Overlay of the backbone of the B1 strand before (cyan) and after refinement (blue/red). The twist and bend angles (defined in *D*) for three frames are shown on the *i* + 1 atom: before refinement, cyan and red, respectively; after refinement, blue and green, respectively. A cartoon representation of the canonical straight and twisted B1 strand is shown on the right. (*D*) Definition of backbone twist and bend angles in a β strand. For four consecutive Cα atoms, we define the midpoints between Cα(*i*)–Cα(*i*+1), Cα(*i*+1)–Cα(*i*+2), Cα(*i*+2)–Cα(*i*+3) as M1, M2, and M3, respectively. P is the midpoint between M1 and M2, and Q is the midpoint between M2 and M3. The twist angle is then defined as the dihedral angle between Cα(*i*+1), P, Q, Cα(*i*+2). The twist angle of the *trans* state is 0°. The bend angle is defined as the angle between the $\overrightarrow{M1M2}$and $\overrightarrow{M2M3}$ vectors. The sign of the bend is negative (positive) when the $\overrightarrow{M2M3}$ projects outside (inside) the plane of the page (32). (*E*–*G*) Agreement between observed and calculated $^1D_{CH}$ (*E* and *F*) and $^1D_{NH}$ (*G*) RDC data for the lowest-energy structure. In *E*, the $^1D_{CH}$ value for the Thr142 Cβ-Hβ bond vector that undergoes an almost 180° rotation upon twisting (*Inset*) is shown in cyan for the straight conformation with the arrow indicating its value in the twisted B1 strand. *F* is a zoomed-in version of *E* showing only $^1D_{CH}$ data for residues in the B1 strand with the corresponding atoms labeled.

20 μM to 1.3 mM (corresponding to 20 to ∼600 μM NMR-visible species).

Several kinetic schemes were examined including simple two-site monomer–dimer and monomer–oligomer exchange, on- and off-pathway three-site exchange, and a four-state exchange model (Table 1). Neither two-site monomer–dimer nor monomer–oligomer models satisfy the experimental data (reduced χ^2 values of 94 and 3.4, respectively; Table 1): The former completely fails to reproduce the experimental data (*SI Appendix*, Fig. S8*A*), while the latter reproduces the ^{15}N-CPMG relaxation dispersion data but not the off-resonance ^{15}N-$R_{1\rho}$ data (*SI Appendix*, Fig. S8*B*). Likewise, a three-state model comprising a ground-state monomeric species, an excited-state monomer, and an oligomeric species does not fit the data (reduced $\chi^2 = 6.6$), failing to reproduce either the ^{15}N-CPMG relaxation dispersion or off-resonance ^{15}N-$R_{1\rho}$ data. An on-pathway three-state model comprising a major monomeric state that interconverts with a sparsely populated dimer that subsequently exchanges with the oligomeric species reproduced the data to a greater extent with reduced χ^2 of 2.4, while a branched scheme in which the dimer is off-pathway and the major monomeric species exchanges with the oligomer results in a somewhat larger reduced χ^2 of 2.8 (*SI Appendix*, *SI Materials and Methods*). The best fit is obtained with a four-state scheme comprising interconverting monomeric (major) and dimeric (minor) states, both of which exchange with the oligomer (reduced $\chi^2 = 2.0$) (Figs. 5 and 6 and *SI Appendix*, Figs. S5–S7). It should be noted that the ^{15}N-CPMG relaxation dispersion and δ_{ex} data largely report on the monomer–dimer interconversion (*SI Appendix*, Fig. S9 *A* and *B*), whereas the ^{15}N-ΔR_2 and off-resonance ^{15}N-$R_{1\rho}$ data are sensitive to the interaction with the high-molecular-weight oligomer (*SI Appendix*, Fig. S9*C*). Indeed, the "inverted" appearance of the ^{15}N off-resonance $R_{1\rho}$ profiles (Fig. 5*B*) is characteristic of an exchange process between NMR-visible and high-molecular-weight, NMR-invisible "dark" species (*SI Appendix*, Fig. S9*C*).

At a concentration of 500 μM NMR-visible CTD species, the ground-state monomer (M) and excited-state dimer (D) exchange at a rate $k_{ex}^{M\leftrightarrow D} \sim 2{,}400\ s^{-1}$ with populations of ∼89% and 7%, respectively; dimers readily interact with a large oligomeric species (forming state DO) with a population of ∼3%, while monomers also bind to the oligomers (state MO), albeit with a lower population of ∼1%. Exchange between dimer and oligomer ($k_{ex}^{D\leftrightarrow DO} \sim 1{,}400\ s^{-1}$) is approximately five times faster than between monomer and oligomer ($k_{ex}^{M\leftrightarrow MO} \sim 255\ s^{-1}$). The apparent forward rate k_1^{app} is linearly dependent upon the concentration of monomer, as expected for a dimerization reaction (36). We assumed that k_3^{app}

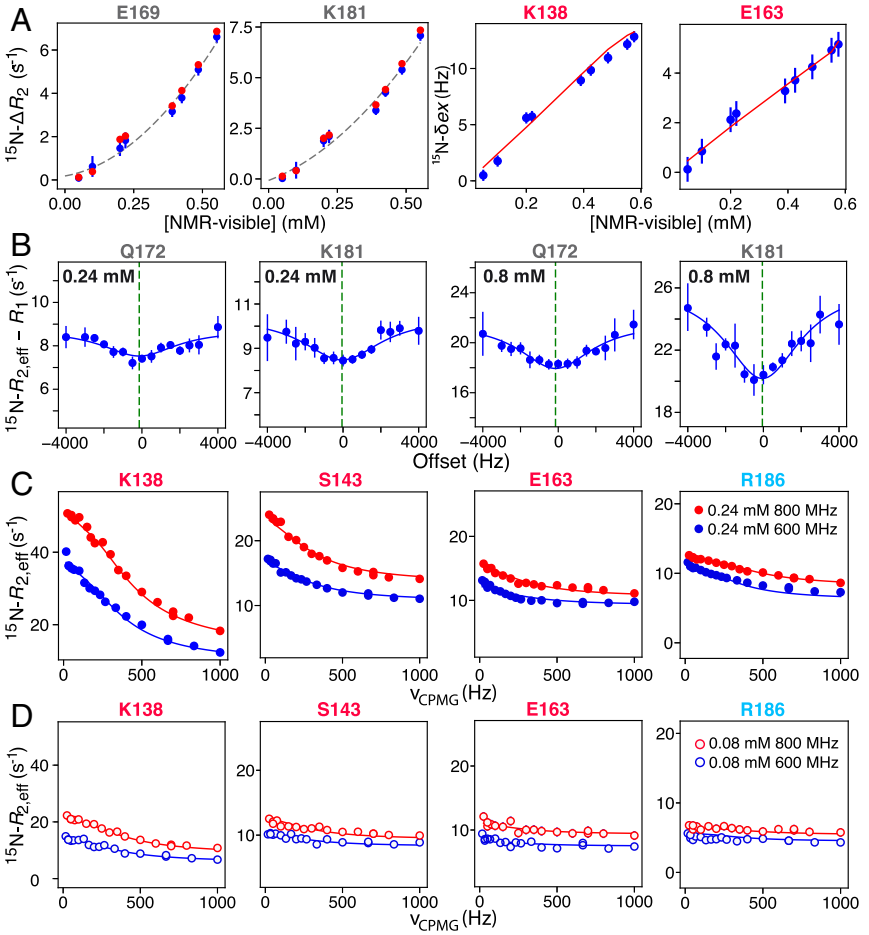

Fig. 5. NMR analysis of the kinetics of concentration-dependent CTD oligomerization at 288 K. (*A*) ^{15}N-ΔR_2 (obtained with a 1.5-kHz spin-lock field) and ^{15}N-exchange induced shifts (δ_{ex}) as a function of NMR-visible CTD concentration. The ^{1}H spectrometer frequency is 600 MHz. (*B*) Off-resonance ^{15}N-$R_{1\rho}$ profiles (2-kHz spin-lock field) as a function of offset from the carrier frequency recorded at two concentrations (0.24 and 0.8 mM) of the NMR-visible CTD species. The offset from the carrier frequency of the ground state monomer is shown as a green line. The ^{1}H spectrometer frequency is 600 MHz. ^{15}N CPMG relaxation dispersion profiles at (*C*) 0.24 and (*D*) 0.8 mM NMR-visible CTD species recorded at 600 (blue) and 800 (red) MHz. All data were recorded on [^{15}N/^{13}C/^{2}H]-labeled CTD. The experimental data in *A*–*D* are shown as circles, while the best fits to the four-state model for monomer–dimer–oligomer interconversion (Table 1, model 6, and Fig. 6*A*) are shown as solid lines except in the case of ΔR_2 (left two panels in *A*) where the best fits are shown as red circles. Note that the calculated dependence of ΔR_2 on concentration is not smooth as k_2^{app} for the M → MO step is optimized for each concentration separately, while k_1^{app} and k_3^{app} are expressed as $2k_1$[M] and k_3[M]^m, respectively (Fig. 6*A*). The range of values of k_2^{app} over the concentration range is too small to permit a treatment similar to that used for k_3^{app}. Residues associated with the ST16/ST17 sites in strand B1 and residues in strand B5 are indicated at the top of each panel in red and cyan, respectively. The dashed lines in the ΔR_2 plots shown in the left two panels of *A* are second-order polynomials to guide the eye. The complete datasets used in the fits are shown in *SI Appendix*, Figs. S5–S7.

scales as the *m*th power of the concentration of NMR-visible species; after global fitting the value of *m* was optimized to a value of ∼1, suggesting a linear relationship between the two quantities. Indeed, in the context of an oligomer whose size increases as the concentration of monomer increases, the number of binding sites on the surface of a spherical oligomer scales approximately linearly with the concentration of NMR-visible monomer within the range of concentrations used (*SI Appendix*, Fig. S4*B*, black line). In this treatment, the M ↔ MO and D ↔ DO transitions are considered as simple binding events of monomers and dimers, respectively, to the surface of the preformed oligomer (i.e., the monomeric and dimeric species that bind to the oligomer surface are the same ones that dissociate from the surface).

For residues that displayed "inverted" ^{15}N off-resonance $R_{1\rho}$ profiles, the chemical shift differences for all transitions were set to zero, as supported by flat ^{15}N CPMG relaxation dispersion profiles (*SI Appendix*, Fig. S7); for the remaining residues the overall chemical shift difference ($\Delta\omega_{M\text{-}DO}$) for the M ↔ D ↔ DO pathway was assumed to be equal to $\Delta\omega_{M\text{-}D} + \Delta\omega_{D\text{-}DO}$, and a two-membered representation was used that preserves the relative signs of $\Delta\omega_{M\text{-}D}$ and $\Delta\omega_{D\text{-}DO}$ (see *SI Appendix* for details) (37). The average $\Delta\omega_{M\text{-}D}$ and $\Delta\omega_{D\text{-}DO}/\Delta\omega_{M\text{-}MO}$ values obtained from the global fits are ∼1.3 and ∼0 ppm, respectively (*SI Appendix*, Table S3).

The average transverse relaxation rates of the oligomer-bound states MO and DO were assumed to be equal, yielding $<^{15}\mathrm{N} - R_2^{\{MD\}O}>$ ∼160 s^{-1}, 20 to 25 times larger than that for the monomeric species M (∼7 s^{-1}), consistent with a particle size of 4 to 5 nm in radius obtained by dynamic light scattering (Fig. 6*B*) and a predicted rotational correlation time (τ_R) of 100 to 130 ns. (It should be noted that the on-pathway three-state model yields a value of $<^{15}\mathrm{N} - R_2^{DO}>$ that is too large [∼300 s^{-1}], while the off-pathway three-state model yields a value of $<^{15}\mathrm{N} - R_2^{MO}>$ that is too small [∼100 s^{-1}]). The population of DO is always larger than that of MO, which only becomes significant at higher concentrations (*SI Appendix*, Fig. S10). The concentration

Table 1. Kinetic models used to analyze the NMR relaxation-based data

Model	Reduced χ^2	
	Wild type	T142A
1. M ⇄ D	94	—
2. M ⇄ MO	3.4	—
3. M ⇄ M^*⇄M^*O	6.6	—
4. *D ⇄ M ⇄ MO*	2.8	7.1
5. *M ⇄ D ⇄ DO*	2.4	5.7
6. *MO ⇄ M ⇄ D ⇄ DO*	2.0	5.1

The best fits shown in Figs. 5–7 of the main text and *SI Appendix*, Figs. S5–S7, S11, S13, and S14 make use of the four-state model (model 6). A summary of the data employed for the wild type and T142A mutant is provided in *SI Appendix*, Table S2.

dependence of the populations of oligomer-bound monomers (MO) and dimers (DO) is consistent with the concentration of NMR-invisible species (*SI Appendix*, Fig. S10).

Transition of Strand B1 from a Twisted to Straight Configuration Leads to Oligomerization. To further investigate the events that lead to oligomerization in structural terms we examined the exchange-induced ^{1}Hα, ^{13}Cα, and ^{13}Cβ shifts as a function of the concentration of NMR-visible CTD at 298 K. At 288 K, the temperature used to acquire the relaxation-based data in Fig. 5, severe chemical exchange line broadening did not allow the observation of many of the S/T ^{1}H-^{13}C cross-peaks within strand B1. At 298 K, however, the signal-to-noise is higher (at least at lower protein concentrations), and exchange line broadening of ^{1}H-^{13}C cross-peaks is reduced by shifting the exchange processes to a faster regime on the chemical shift timescale. The chemical shift titration data for both ^{1}H-^{15}N and ^{1}H-^{13}C resonances belonging to residues in strand B1 scale linearly with concentration, consistent with dimer formation (Fig. 6*C* and *SI Appendix*, Fig. S11), as deduced from the data collected at 288 K.

Downfield shifts ranging from +15 to +32 Hz for ^{1}Hα and ^{13}Cβ resonances and upfield shifts of −10 to −20 Hz for ^{13}Cα resonances are observed for residues in stand B1, consistent with a transition from a twisted conformation to a conformation with more typical β sheet backbone torsion angles (38). Although there is likely some contribution from dimerization to the exchange-induced shifts, the predominant factor influencing ^{13}Cα and ^{13}Cβ exchange-induced shifts originates from secondary shifts due to changes in backbone ϕ/ψ torsion angles accompanying the untwisting of strand B1. The same trend in secondary chemical shifts was also observed for residues in the B2-B3 loop, suggesting that the N- and C-terminal ends of strands B2 and B3, respectively, are extended upon straightening of strand B1, resulting in a structure that resembles the original CS-ROSETTA model (15).

The M-to-D transition in Fig. 6*A* therefore implies that dimerization is accompanied by a conformational interconversion between the twisted and straight conformations of the B1 strand. The chemical shift changes obtained between states D and M then likely result from these conformational changes, while the exchange rate between M and D would be determined by the slowest (rate-limiting) step for this interconversion.

To further investigate the role of strand B1 twisting in CTD oligomerization we mutated Thr142 (which experiences the largest conformational change upon twisting) to alanine. Large ^{1}H$_N$/^{15}N chemical shift changes were only observed for residues in close proximity to Thr142, showing that the mutation to alanine does not affect the overall fold of the CTD domain (*SI Appendix*, Fig. S12). ^{15}N-CPMG relaxation dispersion experiments that almost exclusively report on the monomer–dimer transition show largely diminished profiles for residues in the ST16/ST17 sites (Fig. 7*A* and *SI Appendix*, Fig. S13) compared to the wild-type CTD (Fig. 5*C* and *SI Appendix*, Fig. S7*A*). Global fitting of the ^{15}N-CPMG relaxation dispersion (Fig. 7*A*), off-resonance ^{15}N-$R_{1\rho}$ (Fig. 7*B*), and ^{15}N-ΔR_2 (Fig. 7*C*) data for the T142A CTD mutant (see also *SI Appendix*, Figs. S13 and S14) to the four-state model (Fig. 7*D*) shows that the dimer equilibrium dissociation constant for the T142A mutant (K_{dimer} ~ 28 mM) is increased about 2.5-fold relative to that of wild type (K_{dimer} ~ 11 mM), leading to a lower population of dimer (~3.5% for T142A versus ~7% for wild type at an NMR-visible CTD concentration of 0.5 mM). Interestingly, the affinity of the T142A dimer for the large oligomer is also significantly reduced, resulting in a population of oligomer-bound dimer of ~0.5% compared to 3% for wild type. The population of oligomer-bound T142A monomer (~1%), however, remains essentially unchanged relative to wild type. The average transverse relaxation rate for the T142A oligomeric species O ($<^{15}N - R_2^{\{MD\}O}>$ ~188 s^{-1}) is comparable to that for wild type (163 s^{-1}), indicating that the average size of the oligomer remains effectively unchanged. The ^{15}N-Δω$_{MD}$ values for residues in the B1 strand are twofold smaller in the T142A mutant compared to wild type, while residues elsewhere are largely unaffected (Fig. 7*E* and *SI Appendix*, Table S3). These observations are consistent with a critical role for strand B1 twisting, centered around Thr142 (Fig. 3*C*), in controlling dimer formation and subsequent association with and dissociation from a large oligomeric state. Interestingly, the reduced β strand propensity of alanine relative to threonine (39) in the T142A mutant leads to a decreased population of the excited state dimer (with a straight B1 strand) that is the prelude for oligomerization. Thus the T142A mutant is partially trapped in a nonaggregation-prone conformation, in which the B1 strand is presumably twisted, suggesting a complex H-bonding network between the numerous Ser/Thr residues in this region.

Concluding Remarks

Despite recent advances in de novo protein design, creation of all β proteins remains a challenge, largely due to their propensity to aggregate (40). Here we show how the CTD domain of DNAJB6b remains monomeric at low protein concentrations by avoiding edge-strand association. The mechanisms used by β-rich proteins to avoid self-assembly have been inferred by examining static crystal structures and include the formation of kinks, the incorporation of charged residues, and covering edge strands with flexible loops, among others (33). NMR spectroscopy has been used to directly study the interconversion between a protein folding intermediate that exposes an aggregation-prone edge strand and the soluble native state (41). We show here that the CTD of DNAJB6b avoids edge-strand association by increasing its flexibility toward the C terminus, with strand B5 being essentially unfolded in the monomer, and by a distinct additional twist in strand B1 superposed on the slight right-handed twist of an essentially straight canonical β strand (Fig. 4). The additional twist in strand B1 is fully compatible with hydrogen bonding to the adjacent B2 strand in the monomer but not with the edge strand of another CTD monomer owing to the convex shape the twist creates in strand B1 (33). Importantly, the observed twist in strand B1 is not as profound as those seen in nonassembling β-sheet proteins (33) and therefore the thermodynamic penalty for switching to the canonical β strand conformation is not prohibitive, allowing the CTD to interconvert between ground-state monomeric and sparsely populated dimeric and oligomeric forms. Even though strand twisting is a rare strategy against edge strand aggregation, it allows for reversible interconversion between monomers–oligomers that is not afforded by other protective mechanisms. The abundance of Ser and Thr residues in the ST16/ST17 sites within strand B1 (Fig. 1) suggests that

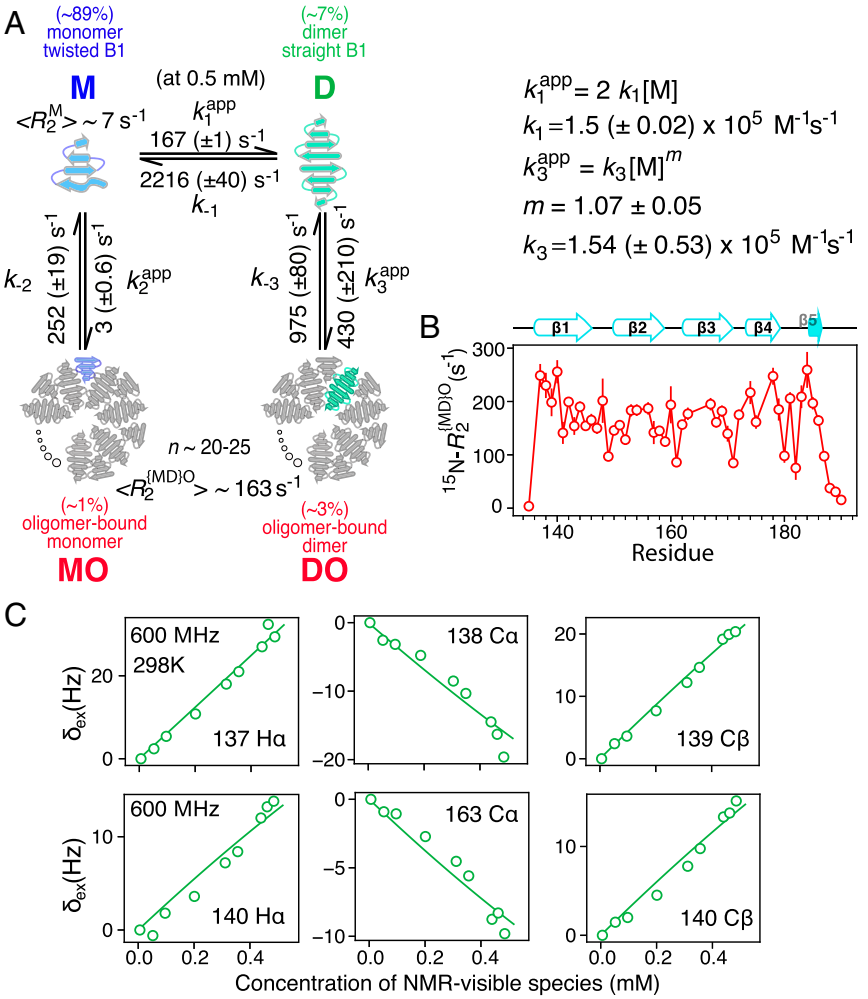

Fig. 6. Transition of B1 to a more regular β-configuration leads to oligomers. (*A*) Kinetic scheme used to fit the experimental NMR data shown in Fig. 5. In the ground-state monomer, M, strand B1 is twisted (Fig. 2*C*). M exchanges with a dimer, D, that adopts a more regular β-conformation as judged by concentration-dependent ^{1}Hα, ^{13}Cα, and ^{13}Cβ chemical changes. Both monomer and dimer exchange with a large-molecular-weight oligomer, O. The latter exchange processes do not relate to the sequential associations that lead to the formation of an oligomer but rather to exchange of a monomer (state MO) or dimer (state DO) unit on the surface of the oligomer with a monomer and dimer, respectively, in solution. Note that $k_1^{app} = 2k_1[M]$, k_3^{app} is expressed as $k_3[M]^m$, and a separate k_2^{app} is optimized for each concentration (*SI Appendix*). (*B*) Plot of optimized ^{15}N-R_2 values for states MO/DO (at 600 MHz) as a function of residue. (*C*) Exchange-induced (δ_{ex}) ^{1}Hα, ^{13}Cα, and ^{13}Cβ shift data as a function of the concentration of NMR-visible CTD recorded at 298 K and 600 MHz. The experimental δ_{ex} values are shown as circles, and the continuous lines represent the fits to the model shown in *A* (*SI Appendix, SI Materials and Methods*). The full δ_{ex} dataset is shown in *SI Appendix*, Fig. S11.

hydrogen bonding involving the side-chain hydroxyl groups of Ser/Thr and backbone amides may stabilize the twisted conformation. If this hypothesis is correct, the above considerations imply that incorporation of Ser and Thr residues in the edge strands of β sheet folds may allow the design of proteins with tuneable self-assembling properties.

It is worth noting that the original structure of the CTD domain, calculated using CS-Rosetta from backbone chemical shifts in conjunction with the very limited set of sparse experimental NMR restraints accessible for the ΔST-DNAJB6b construct (15), did not identify the subtle rearrangements in strand B1 which could only be pinpointed after incorporation of extensive experimental NMR restraints collected on the isolated CTD domain. This is in part due to the sophisticated energy function in CS-Rosetta that is biased toward statistical energy terms, favoring a canonical B1 strand configuration that resembles that in the dimeric and oligomeric forms of the CTD.

The role of the CTD in the chaperone activity of DNAJB6b (42) and the link between DNAJB6b oligomerization and anti-aggregation have been clearly demonstrated both in vivo and in vitro (7, 42). We have previously shown that in the absence of a folded CTD, but in the presence of the ST domain, DNAJB6b is monomeric (15); results presented here demonstrate that the CTD alone can self-assemble, although much less efficiently in the absence of the ST domain. Based on these observations, it is evident that interactions through the CTD domain are vital for DNAJB6b oligomerization but are also critically modulated by the ST domain. Therefore, it is intriguing to hypothesize that twisting and unwinding of the ST16/ST17 sites in strand B1 may be the driving force for subunit exchange in DNAJB6b. Indeed, mutation of the ST16/ST17 sites to alanine, while retaining the oligomeric form of the protein, has a dramatic effect on the ability of DNAJB6b to inhibit amyloid β aggregation (16). This is presumably due to strand B1 being locked in a canonical straight conformation, effectively blocking subunit exchange between various oligomeric states of DNAJB6b that is paramount for inhibition of aggregation (43). Even a single-point mutation (T142A) in that region impacts the association and dissociation rates from the oligomeric species (Fig. 7*D*), which could have a major effect on chaperone activity. In addition, the large heterogeneous oligomers formed by full-length DNAJB6b dissociate to form dimers in the

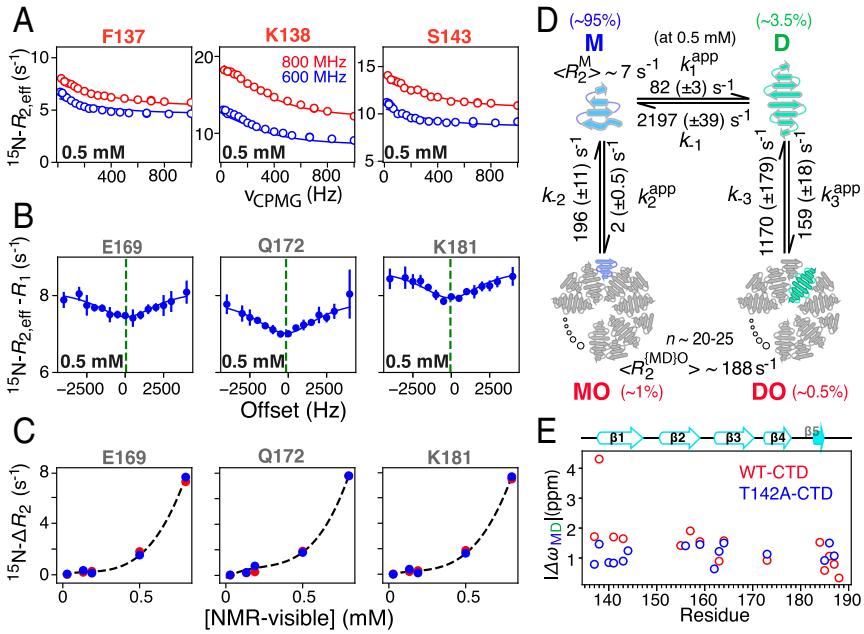

Fig. 7. The T142A mutation within the ST17 site of strand B1 affects CTD oligomerization. (*A*) ^{15}N CPMG relaxation dispersion profiles at 600 (blue circles) and 800 (red circles) MHz recorded for the T142A mutant at an NMR-visible concentration of 0.5 mM. (*B*) Off-resonance ^{15}N-$R_{1\rho}$ profiles (2-kHz spin-lock field) as a function of offset from the carrier frequency recorded at 600 MHz on a T142A sample at an NMR-visible concentration of 0.5 mM. The offset from the carrier frequency of the monomeric ground state is shown as a green line. (*C*) ^{15}N-ΔR_2 profiles (using a 1.5-kHz spin-lock field) profiles as a function of the concentration of the T142A NMR visible species. The experimental data in *A*–*C*, recorded at 288 K, are shown as circles, while the best fits to the four-state model for monomer–dimer–oligomer interconversion (*D*) are shown as solid lines except in the case of ΔR_2 where the best fits are shown as red circles (Fig. 5). The dashed line in *C* serves only to guide the eye. The complete datasets are shown in *SI Appendix*, Figs. S13 and S14. (*D*) Kinetic model used to fit the data with the optimized values of the rate constants. (*E*) Comparison of the fitted $\Delta\omega_{M\text{-}D}$ for wild-type CTD (red) and the T142A mutant (blue). The complete datasets used in the fits are shown in *SI Appendix*, Figs. S13 and S14.

presence of substrates such as amyloid β40 (33), further highlighting the importance of dimeric species for DNAJB6b function.

Interestingly, segments that are rich in Ser/Thr residues have been proposed to control reversible protein self-assembly in phase separation by forming kinked β strands (44) in a manner similar to that whereby the ST16/ST17 sites control reversible oligomerization of CTD. The exact atomic forces that are at the origin of reversible oligomerization will have to be thoroughly investigated and could potentially be manipulated through careful changes in amino acid sequence (45) and/or posttranslational modifications (46). The design of stable monomeric β-rich folds is challenging on its own; the ability, however, to control and predict the oligomerization process may open new avenues for functional protein design.

The role of the ST1–ST15 region of the ST domain (Fig. 1) in full-length DNAJB6b should not be underestimated. ST1–ST15 could potentially modulate the kinetics of monomer–dimer–oligomer exchange shown in Fig. 6*A* by potentially hydrogen bonding to the ST16/ST17 sites, thereby modulating the propensity of ST16/ST17 to twist, or by stabilizing interactions that lead to oligomers through the numerous aromatic residues within the ST domain (Fig. 1). Both scenarios effectively would increase k_1^{app}, k_2^{app}, and k_3^{app} (Fig. 6*A*), shifting the equilibrium toward oligomers rather than the monomer (Fig. 3 *B* and *C*). Further work is needed to elucidate the role of the complete ST domain and any potential JD–CTD interactions (15) to DNAJB6b oligomerization.

In conclusion, our NMR data show that exchange with a conformation in which strand B1 is straight leads to increased rigidity of the "left" side of the β sheet (Fig. 2*B*), leading to edge-strand association through strand B1 that generates an extended layer of β sheet that can readily oligomerize. These data thus reveal a remarkable mechanism mediated by subtle backbone conformational changes within the ST16/ST17 sites in strand B1 that controls the oligomeric state of DNAJB6b. Our findings provide insights for the design of proteins that self-assemble in a tuneable manner and pave the way to an atomic-level understanding of the mechanisms by which DNAJB6b inhibits nucleation events in protein aggregation.

Experimental Methods

Details of protein expression and purification, isotope labeling, sample conditions, NMR experimental details, quantitative analysis of NMR-based relaxation data (CPMG relaxation dispersion, off-resonance $R_{1\rho}$, ΔR_2, and exchange-induced shifts), global fitting procedures, and structure calculations using Xplor-NIH (31) are provided in *SI Appendix*.

Data Availability. Atomic coordinates, experimental restraints, and chemical shift assignments reported in this paper have been deposited in the Protein Data Bank, http://www.wwpdb.org/ (PDB ID code 7JSQ) (47). All the experimental relaxation-based NMR data shown in the *SI Appendix* and used to fit the kinetic models have also been deposited in digital format in Figshare (DOI: 10.6084/m9.figshare.13012682).

ACKNOWLEDGMENTS. We thank Drs. James Baber, Dan Garrett, and Jinfa Ying for technical assistance. This work was supported by the Intramural Program of the National Institute of Diabetes and Digestive and Kidney Diseases at the NIH (to G.M.C., DK029023).

1. P. J. Muchowski, J. L. Wacker, Modulation of neurodegeneration by molecular chaperones. *Nat. Rev. Neurosci.* **6**, 11–22 (2005).
2. F. Chiti, C. M. Dobson, Protein misfolding, amyloid formation, and human disease: A summary of progress over the last decade. *Annu. Rev. Biochem.* **86**, 27–68 (2017).
3. A. Wentink, C. Nussbaum-Krammer, B. Bukau, Modulation of amyloid states by molecular chaperones. *Cold Spring Harb. Perspect. Biol.* **11**, a033969 (2019).
4. Y. E. Kim, M. S. Hipp, A. Bracher, M. Hayer-Hartl, F. U. Hartl, Molecular chaperone functions in protein folding and proteostasis. *Annu. Rev. Biochem.* **82**, 323–355 (2013).

5. H. H. Kampinga, E. A. Craig, The HSP70 chaperone machinery: J proteins as drivers of functional specificity. *Nat. Rev. Mol. Cell Biol.* **11**, 579–592 (2010).
6. M. P. Mayer, B. Bukau, Hsp70 chaperones: Cellular functions and molecular mechanism. *Cell. Mol. Life Sci.* **62**, 670–684 (2005).
7. V. Kakkar *et al*., The S/T-Rich motif in the DNAJB6 chaperone delays polyglutamine aggregation and the onset of disease in a mouse model. *Mol. Cell* **62**, 272–283 (2016).
8. C. Månsson *et al*., Interaction of the molecular chaperone DNAJB6 with growing amyloid-beta 42 (Aβ42) aggregates leads to sub-stoichiometric inhibition of amyloid formation. *J. Biol. Chem.* **289**, 31066–31076 (2014).
9. C. Månsson *et al*., DNAJB6 is a peptide-binding chaperone which can suppress amyloid fibrillation of polyglutamine peptides at substoichiometric molar ratios. *Cell Stress Chaperones* **19**, 227–239 (2014).
10. E. Meng, L. A. Shevde, R. S. Samant, Emerging roles and underlying molecular mechanisms of DNAJB6 in cancer. *Oncotarget* **7**, 53984–53996 (2016).
11. Y. Ding *et al*., Trapping cardiac recessive mutants via expression-based insertional mutagenesis screening. *Circ. Res.* **112**, 606–617 (2013).
12. S. Taguwa *et al*., Defining Hsp70 subnetworks in dengue virus replication reveals key vulnerability in flavivirus infection. *Cell* **163**, 1108–1123 (2015).
13. G. Chen *et al*., Bri2 BRICHOS client specificity and chaperone activity are governed by assembly state. *Nat. Commun.* **8**, 2081 (2017).
14. T. R. Alderson *et al*., Local unfolding of the HSP27 monomer regulates chaperone activity. *Nat. Commun.* **10**, 1068 (2019).
15. T. K. Karamanos, V. Tugarinov, G. M. Clore, Unraveling the structure and dynamics of the human DNAJB6b chaperone by NMR reveals insights into Hsp40-mediated proteostasis. *Proc. Natl. Acad. Sci. U.S.A.* **116**, 21529–21538 (2019).
16. C. Månsson *et al*., Conserved S/T-residues of the human chaperone DNAJB6 are required for effective inhibition of Aβ42 amyloid fibril formation. *Biochemistry* **57**, 4891–4902 (2018).
17. T. K. Karamanos, V. Tugarinov, G. M. Clore, Determining methyl sidechain conformations in a CS-ROSETTA model using methyl ^{1}H-^{13}C residual dipolar couplings. *J. Biomol. NMR* **74**, 111–118 (2020).
18. P. Lundström, P. Vallurupalli, T. L. Religa, F. W. Dahlquist, L. E. Kay, A single-quantum methyl ^{13}C-relaxation dispersion experiment with improved sensitivity. *J. Biomol. NMR* **38**, 79–88 (2007).
19. T. Yuwen, R. Huang, P. Vallurupalli, L. E. Kay, A methyl-TROSY-based ^{1}H relaxation dispersion experiment for studies of conformational exchange in high molecular weight proteins. *Angew. Chem. Int. Ed. Engl.* **58**, 6250–6254 (2019).
20. V. Tugarinov, T. K. Karamanos, G. M. Clore, Magic angle pulse driven separation of degenerate 1H transitions in methyl groups of proteins: Application to studies of methyl axis dynamics. *ChemPhysChem* **21**, 1087–1091 (2020).
21. V. Tugarinov, T. K. Karamanos, A. Ceccon, G. M. Clore, Optimized NMR experiments for the isolation of $I = 1/2$ manifold transitions in methyl groups of proteins. *ChemPhysChem* **21**, 13–19 (2020).
22. D. F. Hansen, L. E. Kay, Determining valine side-chain rotamer conformations in proteins from methyl ^{13}C chemical shifts: Application to the 360 kDa half-proteasome. *J. Am. Chem. Soc.* **133**, 8272–8281 (2011).
23. D. F. Hansen, P. Neudecker, L. E. Kay, Determination of isoleucine side-chain conformations in ground and excited states of proteins from chemical shifts. *J. Am. Chem. Soc.* **132**, 7589–7591 (2010).
24. D. F. Hansen, P. Neudecker, P. Vallurupalli, F. A. A. Mulder, L. E. Kay, Determination of Leu side-chain conformations in excited protein states by NMR relaxation dispersion. *J. Am. Chem. Soc.* **132**, 42–43 (2010).
25. S. C. Lovell, J. M. Word, J. S. Richardson, D. C. Richardson, The penultimate rotamer library. *Proteins* **40**, 389–408 (2000).
26. G. Lipari, A. Szabo, Model-free approach to the interpretation of nuclear magnetic relaxation in macromolecules. 1. Theory and range of validity. *J. Am. Chem. Soc.* **104**, 4546–4559 (1982).
27. N. Tjandra, D. S. Garrett, A. M. Gronenborn, A. Bax, G. M. Clore, Defining long range order in NMR structure determination from the dependence of heteronuclear relaxation times on rotational diffusion anisotropy. *Nat. Struct. Biol.* **4**, 443–449 (1997).
28. G. M. Clore, A. M. Gronenborn, A. Szabo, N. Tjandra, Determining the magnitude of the fully asymmetric diffusion tensor from heteronuclear relaxation data in the absence of structural information. *J. Am. Chem. Soc.* **120**, 4889–4890 (1998).
29. Y. Shen *et al*., Consistent blind protein structure generation from NMR chemical shift data. *Proc. Natl. Acad. Sci. U.S.A.* **105**, 4685–4690 (2008).
30. Y. Shen, F. Delaglio, G. Cornilescu, A. Bax, TALOS+: A hybrid method for predicting protein backbone torsion angles from NMR chemical shifts. *J. Biomol. NMR* **44**, 213–223 (2009).
31. C. D. Schwieters, G. A. Bermejo, G. M. Clore, Xplor-NIH for molecular structure determination from NMR and other data sources. *Protein Sci.* **27**, 26–40 (2018).
32. K. Fujiwara, S. Ebisawa, Y. Watanabe, H. Toda, M. Ikeguchi, Local sequence of protein β-strands influences twist and bend angles. *Proteins* **82**, 1484–1493 (2014).
33. J. S. Richardson, D. C. Richardson, Natural β-sheet proteins use negative design to avoid edge-to-edge aggregation. *Proc. Natl. Acad. Sci. U.S.A.* **99**, 2754–2759 (2002).
34. G. A. Morris, R. Freeman, Enhancement of nuclear magnetic resonance signals by polarization transfer. *J. Am. Chem. Soc.* **101**, 760–762 (1979).
35. T. Yuwen, J. P. Brady, L. E. Kay, Probing conformational exchange in weakly interacting, slowly exchanging protein systems via off-resonance $R_{1\rho}$ experiments: Application to studies of protein phase separation. *J. Am. Chem. Soc.* **140**, 2115–2126 (2018).
36. E. Rennella, A. Sekhar, L. E. Kay, Self-assembly of human profilin-1 detected by Carr-Purcell-Meiboom-Gill nuclear magnetic resonance (CPMG NMR) spectroscopy. *Biochemistry* **56**, 692–703 (2017).
37. M. Cai *et al*., Probing transient excited states of the bacterial cell division regulator MinE by relaxation dispersion NMR spectroscopy. *Proc. Natl. Acad. Sci. U.S.A.* **116**, 25446–25455 (2019).
38. D. S. Wishart, B. D. Sykes, The ^{13}C chemical-shift index: A simple method for the identification of protein secondary structure using ^{13}C chemical-shift data. *J. Biomol. NMR* **4**, 171–180 (1994).
39. A. G. Street, S. L. Mayo, Intrinsic beta-sheet propensities result from van der Waals interactions between side chains and the local backbone. *Proc. Natl. Acad. Sci. U.S.A.* **96**, 9074–9076 (1999).
40. E. Marcos *et al*., De novo design of a non-local β-sheet protein with high stability and accuracy. *Nat. Struct. Mol. Biol.* **25**, 1028–1034 (2018).
41. P. Neudecker *et al*., Structure of an intermediate state in protein folding and aggregation. *Science* **336**, 362–366 (2012).
42. J. Hageman *et al*., A DNAJB chaperone subfamily with HDAC-dependent activities suppresses toxic protein aggregation. *Mol. Cell* **37**, 355–369 (2010).
43. N. Österlund, M. Lundqvist, L. L. Ilag, A. Gräslund, C. Emanuelsson, Amyloid-β oligomers are captured by the DNAJB6 chaperone: Direct detection of interactions that can prevent primary nucleation. *J. Biol. Chem.* **295**, 8135–8144 (2020).
44. M. P. Hughes *et al*., Atomic structures of low-complexity protein segments reveal kinked β sheets that assemble networks. *Science* **359**, 698–701 (2018).
45. A. G. Cochran, N. J. Skelton, M. A. Starovasnik, Tryptophan zippers: Stable, monomeric beta -hairpins. *Proc. Natl. Acad. Sci. U.S.A.* **98**, 5578–5583 (2001).
46. D. Ghosh, P. Lahiri, H. Verma, S. Mukherjee, J. Chatterjee, Engineering β-sheets employing *N*-methylated heterochiral amino acids. *Chem. Sci. (Camb.)* **7**, 5212–5218 (2016).
47. T. Karamanos, V. Tugarinov, G. M. Clore, Refined structure of the C-terminal domain of DNAJB6b. Protein Data Bank. https://www.rcsb.org.structure/7JSQ. Deposited 21 September 2020.